OBSERVED SEASONAL AND TIDAL VARIABILITY OF SEA LEVEL AND CURRENT ON THE ANDAMAN SHELF

Chalermrat Sangmanee[1], Jingsong Guo[2], Yuhuan Xue[2], Fangli Qiao[2] and Somkiat Khokiattiwong[3]

[1] *Phuket Marine Biological Center, Mueang Phuket District, Phuket 83000, Thailand*
[2] *The First Institute of Oceanography, Ministry of Natural Resources, Qingdao 266061, China*
[3] *IOC Sub-Commission for the Western Pacific, Government Complex B, Bangkok 10210, Thailand*
Corresponding author: csangmanee@gmail.com

ABSTRACT: The Andaman shelf is a broad continental shelf extending in a north-south direction along the eastern boundary of the Andaman Sea (AS). While the Andaman shelf has been investigated for a long time, the fundamental understanding on the shelf dynamics is still limited largely due to the scarcity of long-term oceanographic observation. Under a collaborative framework between Thailand and China, an Acoustic Doppler Current Profiler (ADCP) was deployed on the shelf for a year, providing year-round in situ observation. By analyzing the ADCP and tide-gauge observations, the sea level and current variations on seasonal and tidal timescales were investigated during the study period. Our analyses showed a clear seasonal pattern of sea level corresponding to monsoon winds. Current, in contrary, exhibited a weak seasonality and were likely influenced by remote forcings from the Equatorial Indian Ocean (EIO). Our observation highlights the connection between the AS and the EIO. In addition, tides are semi-diurnal with M_2 and S_2 being the most predominant tidal constituents, followed by N_2 and K_1. Tidal currents for the two major constituents exhibited a clockwise rotation with major semi-axis lengths oriented toward north-eastward direction.

Keywords: Andaman Sea, Seasonal variation, Tide, current

INTRODUCTION

The Andaman shelf is a broad continental shelf (~140 km from the coast to 500 m depth) extending in a north-south direction from 6°N to 15°N along the eastern Andaman Sea (AS), part of East Indian Ocean. Circulation in the AS can be complicated due to local forcings, Asian monsoon, and remote forcing from Indian Ocean (Clarke and Liu 1993; Chaterjee *et al.* 2017). On the Andaman shelf, the Asian monsoons characterized by a seasonal reversal of wind (*i.e.*, northeasterly wind during November–March and southwesterly during June–September) induces the flow in along-shelf direction, which is attributable to Ekman transport and the geostrophic relationship. Such a mechanism has been discussed thoroughly on west Florida shelf where is also influenced by seasonal reversal wind system (*e.g.*, Yang and Weisberg 1999; Liu and Weisberg 2005; Carlson and Clarke 2009). Along-shelf wind stress setting up along-shelf current can be effective especially on the inner shelf region (Liu and Weisberg 2005).

Equatorial response enters the AS through the Great Channel (Clarke and Liu 1993; Chaterjee *et al.* 2017). This is related to zonal equatorial wind in the Indian Ocean inducing net meridional transport, and generating eastward propagating Kelvin waves (Clarke and Liu 1993). Once striking Sumatra Island, wave energy is trapped to the eastern boundary, forming poleward propagating coastal Kelvin wave (McCreary 1976; Clarke 1983). Since the width of the Great Channel is about the 1st baroclinic Rossby radius of deformation (~200 km) (Chelton *et al.* 1998), a passage of wave can travel into the AS. This in turn induces coastal sea level along the travelling path of the passage. Equatorial response can be influential to the AS especially at semi-annual timescale (Clarke and Liu 1993).

Tide, considered to be a high-frequency process, plays significant roles in the AS. Past studies suggest its contribution to the generation of internal waves (*e.g.*, Yi-Neng *et al.* 2012; Mohanty *et al.* 2018; Peng *et al.* 2021), which affects marine ecosystems (Walls *et al.* 2012; Walls *et al.* 2015). It is suggested that M_2 and S_2 are dominant tidal constituents in

the AS (Angsakul *et al.* 2007; Liu *et al.* 2018a). Major semi-axes of the tidal current for M_2 and S_2 are about 7–9 cm/s and 3–4 cm/s respectively. Unlike semi-diurnal constituents, diurnal constituents are weak, and shallow water tides are negligible (Liu *et al.* 2018a).

These past studies about the current were largely based on indirect observation such as sea surface heights (*e.g.*, Clarke and Liu 1993; Bonjean *et al.* 2002), and numerical simulation (Chaterjee *et al.* 2017). Therefore, direct observation is critically needed for verification. For the first time, long observation was conducted in the central AS (Liu *et al.* 2018a; Liu *et al.* 2018b), showing inconsistencies between observations and numerical results in some months (Liu *et al.* 2018a). Though agreements with the surface current derived using a diagnostic model (Bonjean *et al.* 2002) was reported (Liu *et al.* 2018a), altimetry data can be complicated by signals of unresolved high-frequency variabilities on the shelf (Gille and Hughes 2001; Volkov *et al.* 2007). As we are interested in the shelf region where the dynamics is highly influenced by topography, direct measurement of the shelf current is necessary. Under an international collaboration between Thailand and China, an Acoustic Doppler Current Profiler (ADCP) was deployed on the Andaman shelf and continuously collected data year-round. Based on the products obtained under this collaboration including the observations from other sources (*e.g.*, tide-gauge sea level and discrete observation using Conductivity-Temperature-Depth (CTD)), understanding on the shelf circulation and dynamics are greatly enhanced.

Our aims for this study are to examine current on the Andaman shelf including low-frequency and tidal currents based on the year-round observation from the bottom-moored ADCP. Sea level measurements from a tide gauge and that estimated from the depth measurements derived from the ADCP are analyzed to obtain the sea level variation on the shelf including tide. In addition, water mass characteristics are described based on hydrographic observations using CTD instrument cast in nearby locations.

MATERIAL AND METHOD

Meteorological data

10-meter wind components and surface pressure reanalysis of National Centers for Environmental Prediction (NCEP) (Kalnay *et al.* 1996), provided by the NOAA/OAR/ESRL PSL, Boulder, Colorado, USA (https://psl.noaa.gov/data/gridded/data.ncep. reanalysis.surface. html) are used in this study. The data has a 2.5° spatial resolution and a 6-hour time interval. We extracted the data within two rectangular domains, *i.e.*, 6.25°N–11.25°N and 96.25°E–98.75°E, and 2°S–2°N and 84°E–94°E. The first domain is located in the AS, and the latter domain is located in the Eastern EIO (EEIO) (Fig. 1). Data treatments included spatial averaging for each time step

We estimated the wind stress components by using following quadratic function:

$$\tau_x = \rho_a C_D u_w \left| \vec{V}_w \right| \qquad (1)$$

where τ_x is zonal wind stress, ρ_a is air density (1.2 kg/m³), C_D is drag coefficient (1x10⁻³), u_w is zonal wind speed, and $\left| \vec{V}_w \right|$ is magnitude equivalent to $\sqrt{u_w^2 + v_w^2}$. In meridional direction, τ_x is replaced by τ_y, and u_w is replaced by v_w

Currents

Teledyne Marine 300-kHz Workhouse Sentinel ADCP was deployed at 8.576°N and 97.545°E (see Fig. 1) during December 11, 2018 – November 10, 2019. It was moored on the seafloor at the depth about 120 m with upward-looking transducers. We configured the ADCP to measure velocity components every 10 minutes at 4-meter bins in vertical distance with the blank of 6.24 meters. In addition to velocity profiles, it measured the water pressure which can be interpreted as the distance between the instrument and the sea surface. The pre-analysis of the measurements included resampling 10-minutes interval data into hourly measurement.

The ADCP measured velocity components at fixed distances above its transducers, but the instrument depth varies in time. Hence, the distance between the sea surface and the depth at which velocity was measured also varies in time. This can be estimated by the expression, *h - (6.24 + 4b)*, where *b* is bin number and *h* is the instrument depth. To obtain velocities at fixed levels referenced to sea surface, we, for each time step, projected original velocity profile onto reference levels using linear interpolation, and then reconstructed new time series using interpolated values from all time steps.
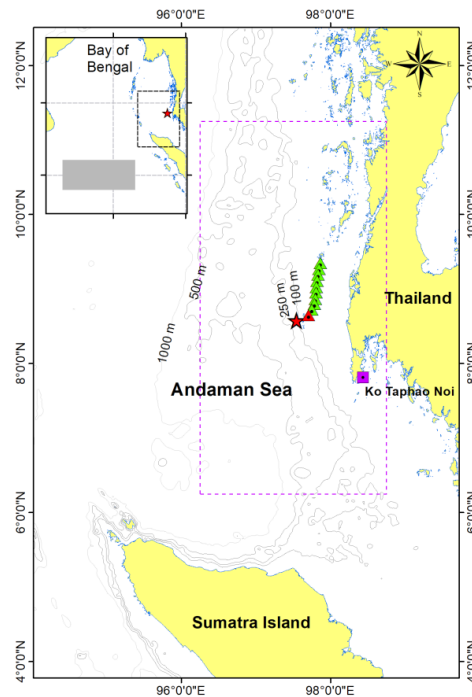
Figure 1. Map and bathymetry of the study area in the Andaman Sea. Grey lines represent 100 m, 250 m, 500 m, and 1000 m isobaths while the red star is the deployment location of our ADCP, the triangles show the CTD stations, and the square is Taphao Noi Island tide gauge location. The rectangular box outlined with purple dash lines is the main study area in the AS (6.25°N–11.25°N and 96.25°N–98.75°N), whereas the grey-shaded box in the inset is in the East Indian Ocean (2°S–2°N and 84°E–94°E).

To separate tidal signal from signals of which timescales are longer than tide, the reconstructed time series was filtered using Godin-type filter (Godin 1972). In practice, we applied 24-point moving average twice and 25-point moving average once, to the reconstructed measurements for each velocity components (u, v) separately. Since Godin-type filter is effective at removing all daily tidal period energy except for the leakage in diurnal frequency band (Emery and Thomson 1997), decomposition using this filter yields de-tided velocity measurements. Therefore, tidal current was obtained by subtracting de-tided values from reconstructed time series. De-tided velocity with respect to depth and time was simply visualized by using stick plot together with the plots of de-tided sea level, and wind stress components.

Rotary spectral estimation, used in tidal current analysis, is based on separation of velocity vector for a specified frequency into clockwise (+) and counterclockwise (-) rotating circular components with amplitudes A^+, A^- and relatives phases θ^+, θ^- respectively (Emery and Thomson, 1997). The method is used in current analysis in many studies (*e.g.*, O'Brien and Pillsbury 1974; Gilmour 1987; Elipot and Lumpkin 2008; Ghaffari and Chegini 2010). In this paper, we followed calculation based on derivation given in Emery and Thomson (1997) (see Chapter 5 in their book for more detail). For each discrete frequency, spectral energy S^+ and S^-, are given by

$$S^+ = \left(A^+\right)^2 \Big/ N\Delta t \tag{2}$$

$$S^- = \left(A^-\right)^2 \Big/ N\Delta t \tag{3}$$

where $N\Delta t$ is the length of measurement. In addition, rotational property of the flow is determined by rotary coefficient r written as

$$r = \frac{\left(S^+ - S^-\right)}{\left(S^+ + S^-\right)} \qquad (4)$$

where r ranges from -1 for clockwise rotation to 0 for unidirectional flow, and to +1 for counterclockwise motion. Analysis was done separately between Northeast monsoon (NEM) and Southwest monsoon (SWM) seasons. To be more precise, we selected measurements during mid-December to mid-March to represent NEM season, and during June–August to represent SWM season.

Smoothing process is necessary in removing noise accompanying the measurement and causing interference by spikes on power spectra. We smoothed the curve using Welch's method (Welch 1967). In more detail, we split measurement into five segments each of which has 50% overlap with preceding and succeeding segments, and then applied the Welch window for each segment (Welch 1967). As a result, the equivalent degree of freedom increases to approximately 10. The resultant spectra from all windows were averaged to obtain representative spectra for frequencies.

Sea level

There are two datasets used in sea level analysis. Tide-gauge data at Taphao Noi Island, Thailand, is provided by University at Hawaii Sea Level Center (UHSLC) dataset (Caldwell *et al.* 2015) at https://uhslc.soest.hawaii.edu/datainfo/. We selected research quality dataset archived by the National Oceanic and Atmospheric Administration (NOAA) National Centers for Environmental Information as the Joint Archive for Sea Level. The other is sea level derived from ADCP depth measurements.

To estimate sea level using ADCP depth measurements, each depth measurement (h) was subtracted from time-averaged depth ($\overline{h}$) obtained by averaging h over the observation period. In other word,

$$h' = h - \overline{h} \qquad (5)$$

Since ADCP is positioned at nearly fixed distance from the seafloor, the distance of the instrument relative to sea surface largely depends on sea surface variation. Hence, we may write

$$\eta_a = h' \qquad (6)$$

where η_a is sea level estimate. We note that this may not be the case for deep-water mooring array as buoyancy perturbation can cause large vertical displacement of the ADCP buoyancy buoy especially in the AS where internal solitary wave is energetic.

Both tide-gauge and ADCP-derived sea levels were adjusted for inverted barometric effect using

$$\eta = \eta_a + \left(P - \overline{P}\right)/\rho_s g \qquad (7)$$

where η is adjusted sea level, η_a is actual sea level, P is surface pressure obtained from NCEP dataset, $\overline{P}$ is time-averaged surface pressure, ρ_s is surface seawater density (1020 kg/m³), and g is gravitational acceleration (9.81 m/s²).

To examine tidal characteristics, we applied spectral estimation method that is based on Fast Fourier Transform (FFT). FFT functions in transforming discrete measurements from time domain into frequency domain in which strengths for each frequency are determined by associated power spectra defined as a square of amplitudes. For deterministic waveform such as tide, spectral analysis is a powerful method.

Hydrographic data

RINKO-Profiler model ASTD102 of JFE Advantech was casted during November 26–29, 2018, and April 7–10, 2019 in nearby locations to ADCP-mooring station (Fig. 1). Temperature and salinity were retrieved from the CTD, while the density was calculated using Gibbs SeaWater oceanographic toolbox (McDougall and Barger 2011). Temperature-Salinity (T-S) diagram and profiles are utilized to describe water characteristics on the Andaman shelf.

Concurrently, the square of buoyancy frequency (N^2) was calculated by using

$$N^2 = -\frac{g}{\rho_0} \frac{\partial \rho}{\partial z} \qquad (8)$$

where ρ is seawater density, ρ_0 is reference seawater density (1020 kg/m³), and $\partial/\partial z$ is partial derivative with depth. We estimated $\partial \rho / \partial z$ by using least square method. This parameter can be used as a measure of stratification of a fluid.

RESULTS AND DISCUSSION

Wind

Asian monsoon prevails over the AS. It is characterized by seasonal change in atmospheric circulation that regulates the climate over Southeast Asia mainland. Figure 2 illustrates NCEP zonal and meridional wind speeds over the study area (Fig. 1). A seasonal pattern is apparent with northeasterly wind lasting from December 2018 to mid-March 2019 and southwesterly wind lasting from June to late-September 2019 (Fig. 2). During the observation period, the maximum daily wind speed at 11 m/s was marked in August.
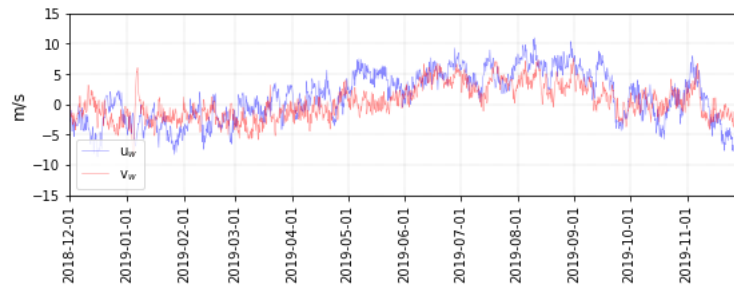
Figure 2. Zonal and meridional wind speeds within rectangular box of 6.25°N–11.25°N and 96.25°N–98.75°N (see area in Fig. 1)

Sea level

De-tided sea levels vary between -40 and 40 cm, being above average during May–August and below the average during September–November and January–March. The standard deviations (SD) are larger at the ADCP-mooring station (13 cm) compared to that at Taphao Noi Island station (9.3 cm). This seasonal pattern is clear especially at the coastal station and is tightly linked to monsoon wind. This can be explained by current-setup sea level along the coast. Along the eastern boundary, the coastline is nearly north-south, thus meridional wind stress could be more influential in current-setup sea level. Seasonally, southerly wind prevails over the AS from May to mid-September, inducing onshore transport, elevating coastal sea level during SWM season. Northerly wind, on the other hand, lowered sea level during January–February as offshore transport (Fig. 3a and 3c).

Though monsoon wind is northeasterly, a remarkably positive sea level was observed in December when sea level increased sharply by 20–40 cm, and then dropped back down a week later (Fig. 3c). Since the wind is northerly locally, the observation disagrees with aforementioned theory. The previous study suggests that fluctuation in coastal sea level along the coast is also related to Indian Ocean (Clarke and Liu 1993). Therefore, examining zonal equatorial wind stress is required in this case.

In early December, westerly equatorial zonal wind burst happened over EEIO. Net equatorward transport is induced when the zonal equatorial wind is westerly, elevating sea level along the equator while concurrently lowering the thermocline layer. As a result, downwelling equatorial Kelvin wave is generated and propagates eastward. Since the 1st baroclinic phase speed is approximately 2.8 m/s (Chelton *et al.* 1998), it could take about 1–2 weeks before the wave reaching the AS. Our observation indicates elevated sea level a week after the burst of eastward wind stress (Fig. 3b) which is in agreement with the theory. This wind burst is also found in February, but not as pronounced as that occurring in December. Wind burst generating equatorial Kelvin wave was also reported elsewhere including in the western equatorial Pacific Ocean (Delcroix *et al.*1993).

Current

The current on Andaman shelf is primarily in north-south orientation and baroclinic-like in structure (Fig. 3d). We observe velocity spin at depth around 40–50 m (Fig. 3d). Since meridional velocity shear is mostly prominent at approximately 50 m (Fig. 4), we calculated depth-averaged velocity

within 20–50 m in order to explain the flow in the upper layer. Depth-average current shows weak seasonality with intermittent reversal (Fig. 5). Southward current is typical during NEM season with strongest current marked in January. Northward current, on the other hand, is not as distinct during SWM season. Conceptually, northerly wind could locally induce southward current, but southerly wind causes northward current along the eastern boundary. This could be effective especially in the inner shelf area. On the other hand, deep ocean forcing complicates the circulation in the outer shelf area like the observation on West Florida Shelf (Liu and Weisberg 2005) and our location. We observed northward flow only in June and July before the current turned southward again in October. Another feature to be remarked is the flow below 70 m. Unlike the flow in the upper layer, it is nearly constantly northward throughout the observation period (Fig. 3).

Strong northward flow is marked in December (Figs. 3 and 5) with the speeds as fast as 40 cm/s persisting for a week. However, this flow does not go in the same direction as what might have been predicted by the local wind direction. We attributed this to the equatorial East Indian Ocean response. Zonal equatorial wind stress can modify the upper ocean in EEIO, generating eastward propagating wave, and inducing northward flow along the Andaman shelf. This is associated with elevating coastal sea level (Fig. 3c). Narrow-band northward flow was also observed in early May (Fig. 5) while there was no distinct eastward equatorial zonal wind stress observed over EEIO and local wind was weak during that time period (Fig. 3). The origin of this flow might be farther westward or is related to the resonance as described in Clarke and Liu (1993). Thus, it leaves us with a question for future investigation.
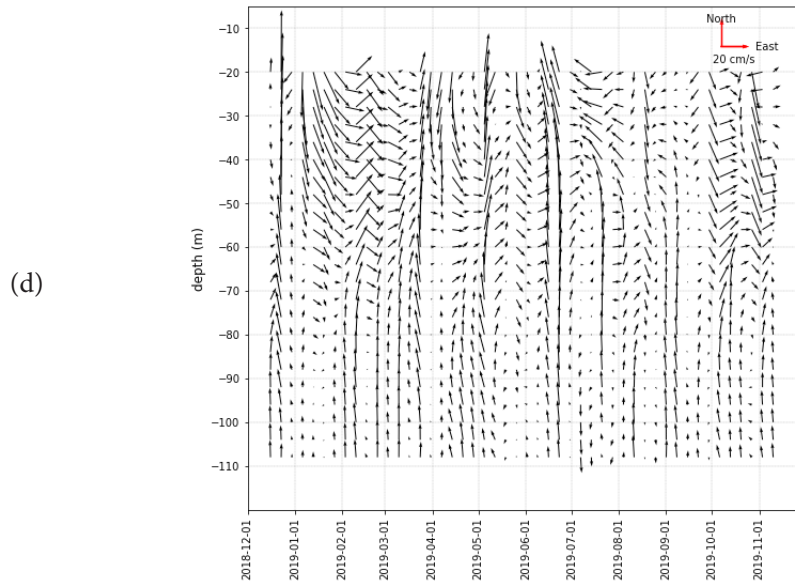
(a)

(b)

(c)

(d)
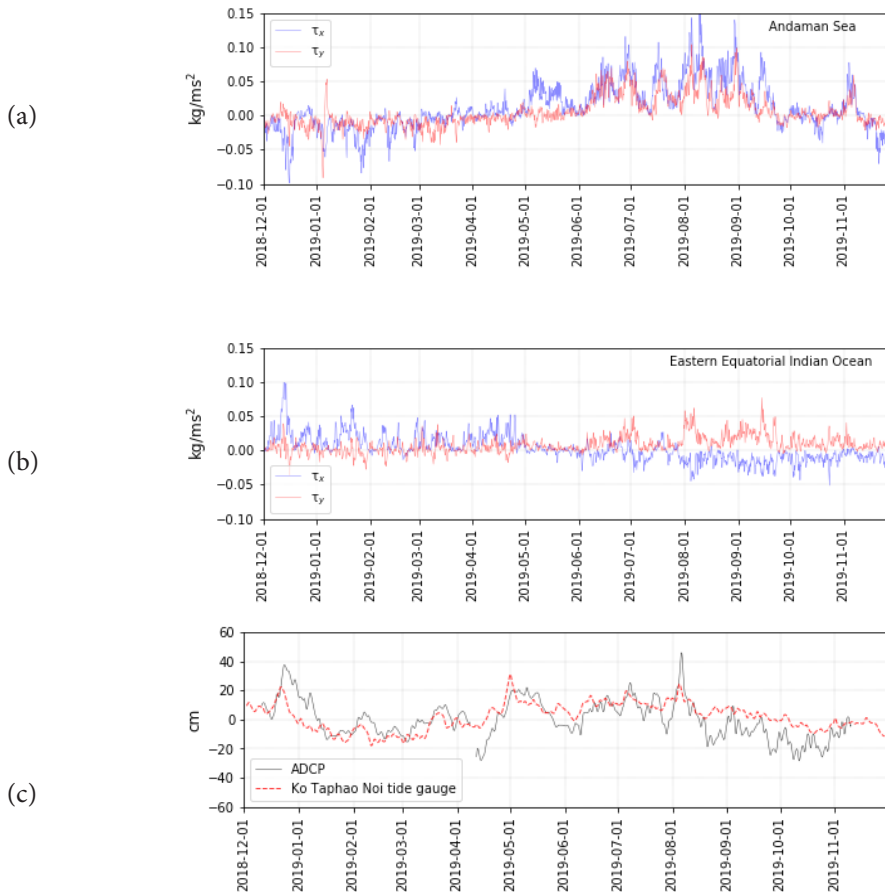
Figure 3. (a) Stress components in Andaman Sea from December, 2018 to November, 2019, and (b) in the Eastern Equatorial Indian Ocean (blue and red lines denote zonal and meridional components respectively), (c) de-tided sea level at ADCP-mooring station (black solid line) and at Taphao Noi Island (red dash line), and (d) weekly velocity stick plot with depth at ADCP-mooring station.
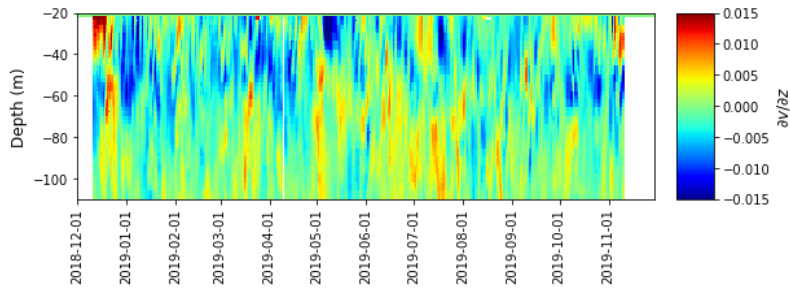

Figure 4. Meridional velocity shears of daily meridional velocity at ADCP-mooring station derived using least square method.
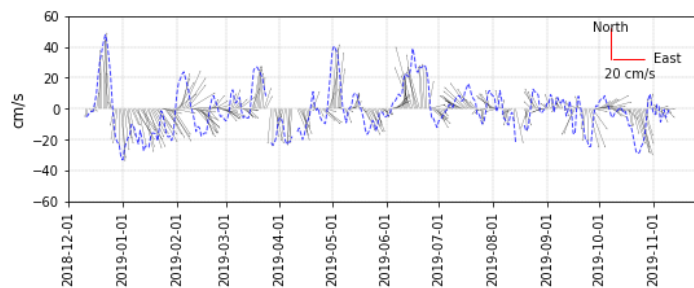

Figure 5. Stick plot of daily depth-averaged velocity for 20–50 m at ADCP-mooring station, and meridional component of the current speed (blue dash line).

Water characteristics

T-S diagram reveals different characteristic in water masses between observations in November and April (Fig. 6). In November, temperature is between 24.8–30.0°C, salinity is 31.6–33.8, and density is 1019.3–1022.4 kg/m³. In April, salinity increases to 32.8–34.5, and water density increases to 1019.6–1024.3 kg/m³. Two features are apparent in the diagram, *i.e.*, near-surface low-salinity water (<32) in November and high-density water (>1022.5 kg/m³) in April. Precipitation is high along southwestern Malaysian Peninsula especially during the last quarter of a year (see Fig. 1 in Wong *et al.* 2016), supplying fresh water locally. The largest river input from the north (*e.g.*, Irrawaddy River) supplies fresh water that accumulates in the AS, and is then transported southward (Mahadevan *et al.* 2016). Hence, we ascribe the decreasing salinity in November to freshwater discharge from land both locally along the western Malaysia Peninsula and remotely from the north. High-density water in lower part of water columns is typical during March–May (Sangmanee *et al.* 2020). It is probably sustained by shallower isothermal layer and a thinner barrier layer from winter to spring (Liu *et al.* 2018b).

Hydrographic profiles at the southernmost CTD-casting station were used to illustrate the water column structures near the ADCP-mooring station. In November, temperature is nearly constant throughout the water column (Fig. 7). The mixed-layer depth (MLD) is the depth at which the temperature changes from the surface temperature by 0.5°C (Levitus 1982). In this study, instead of comparing with the surface temperature we referenced it to 10-meter temperature, thus the MLD was determined at 31 m. This agrees with previous observation in the central AS during the same period of a year (Liu *et al.* 2018a). Considering square of buoyancy frequency (N^2), the N^2 profiles resemble both the temperature and salinity structures. Dominant stratification is marked at 50 m (Fig. 7). In April, stepwise structures of temperature and salinity are apparent in Figure 7b. Two-step stratification is perceived at 30 m and 50 m, corresponding to temperature and salinity patterns (Fig. 7b). We observe shallower MLD in April (18 m) and sharp decline of temperature that likely indicates the beginning of thermocline layer at 50 m, coincided with the typical depth for prominent meridional velocity shear (Fig. 4).

Competitive contribution between temperature and salinity on stratification is examined by using linear equation of state:

$$\rho = \rho_s \left(1 - \alpha_T T' + \beta_s S'\right) \qquad (6)$$

where ρ_s is surface seawater density, T' and S' are water temperature and salinity deviated from the surface, α_T is thermal expansion coefficient (3.1 x 10⁻⁴ K⁻¹), and β_s is saline contraction coefficient (7.2 x 10⁻⁴). Given T' and S' equal to 3.9°C and 1.6 respectively in November (10.8°C and 1.5 in April), results suggest that temperature and salinity comparably contribute to stratification in November (49% and 51% respectively), but temperature dominates stratification in April (76%).
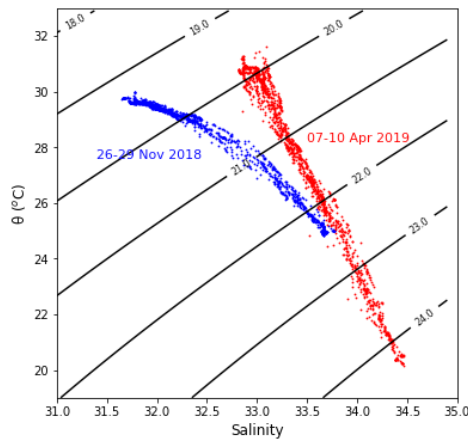

Figure 6. Temperature-Salinity (T-S) diagram plotted using measurements on Andaman shelf (see green triangle symbols in Fig. 1), during November 26–29, 2018 (blue dots), during April 7–10, 2019 (red dots).

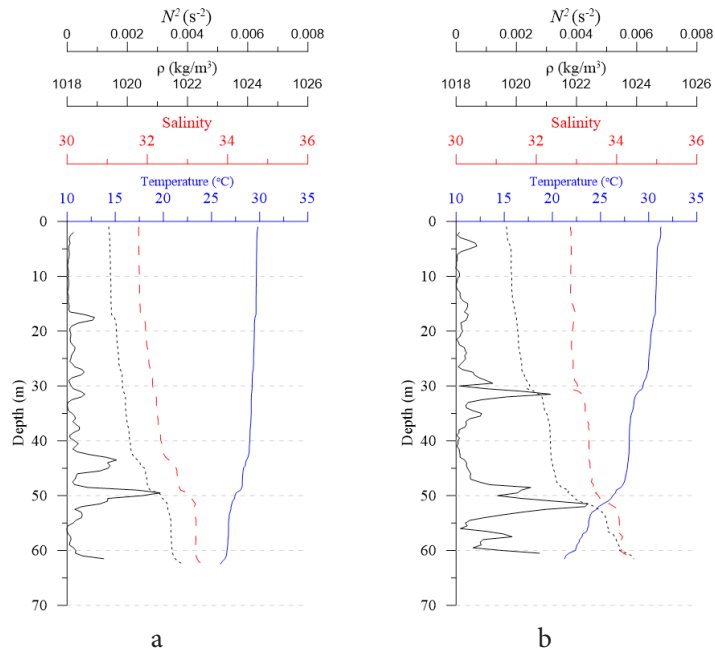*Observed seasonal and tidal variability of sea level and current*

Figure 7. (a) Salinity, temperature (°C), density (kg/m3), and square of buoyancy frequency on November 26, 2018; and (b) on April 7, 2019 at southernmost CTD casting station (see red triangle in Fig. 1).

Table 1. Amplitudes in centimeters of tidal constituents O_1, K_1, N_2, M_2, S_2, and M_4 resolved from observations at ADCP-mooring station and Taphao Noi Island tide gauge during Northeast monsoon (NEM) and Southwest monsoon (SWM) seasons

Constituents	Period (hours)	NEM season		SWM season	
		ADCP	Tide gauge	ADCP	Tide gauge
O_1	25.82	3.1	3.7	4.1	4.3
K_1	23.93	13.0	13.6	15.3	14.2
N_2	12.66	13.1	15.9	10.6	11.6
M_2	12.42	67.3	79.5	67.1	79.7
S_2	12.00	32.1	39.1	30.7	33.9
M_4	6.21	0.8	0.8	1.3	1.2

Tide and tidal current

Tide on the Andaman shelf is semi-diurnal. Tidal ranges are approximately 3.34 m at Taphao Noi Island, and 3.46 m at ADCP station. M_2 tide is the most predominant constituent on the shelf, followed by S_2 tide. M_2 tidal amplitude is twofold amplitude of S_2 tide (Fig. 8 and Table 1). N_2 and K_1 tides contribute equally to the observation, both amplitudes of which are about half of S_2 tidal amplitude. We note that S_2, N_2, and O_1 peaks are not clearly seen in Figure 8. Their disguises in the spectra probably results from spectral leakage and the smoothing process, which results in broad spectra around M_2 and K_1 frequencies.

In addition to the main constituents, shallow water tidal constituents are also observed, *i.e.*, M_4, M_6, and MK_3 (Fig. 8). We omitted M_6 and MK_3 in our discussion but M_4 as the largest of the quarter-diurnal tides generated in shallow water. M_4 tide, a shallow water overtide of principal lunar constituent, can contribute up to 50 cm in amplitude on the shelf (Andersen 1999), but less than a few millimeters in the deep ocean (Ray 2007). It is a pure second harmonic of the principal lunar tide with period of 6.21 hours, and is formed in shallow water (Le Provost 1991; Walters and Werner 1991). We observe the peaks of this constituent in both locations, but its contribution to the sea level are likely negligible (~1 cm).
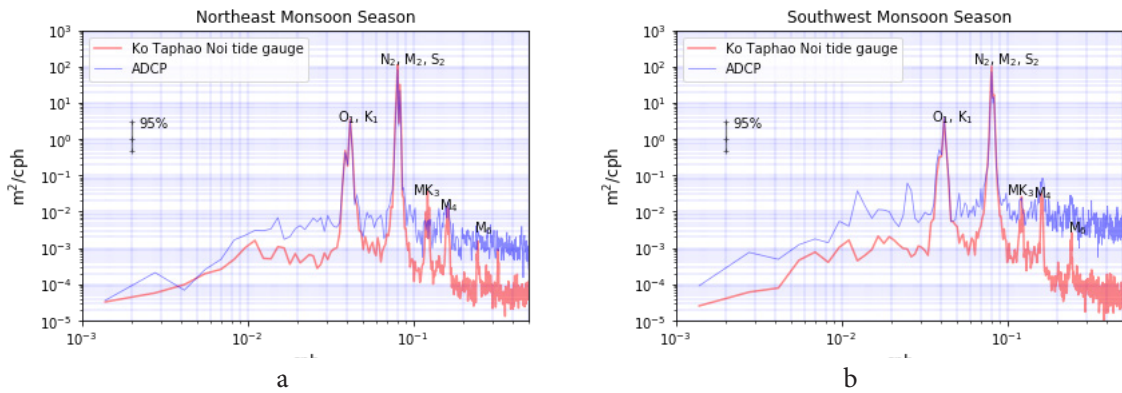

Figure 8. (a) Power Spectral Density (PSD) of high-pass filtered sea level during Northeast monsoon (left) and Southwest monsoon seasons (right) with texts label tidal constituent species.

Table 2. Major semi-axis length (cm/s) for tidal constituents O_1, K_1, N_2, M_2, S_2, and M_4

Depths (m)	NEM season						SWM season					
	O_1	K_1	N_2	M_2	S_2	M_4	O_1	K_1	N_2	M_2	S_2	M_4
20	1.2	2.5	3.5	11.1	5.6	0.9	1.5	3.0	3.2	12.9	4.9	0.2
40	0.6	1.9	1.9	10.8	3.9	0.5	1.4	3.6	3.3	11.2	3.6	0.6
60	0.9	1.6	0.9	7.8	2.9	0.8	0.9	3.1	2.8	8.1	3.0	0.7
80	0.8	1.5	1.1	5.4	3.6	0.5	1.3	3.2	2.1	6.3	1.9	0.6
100	0.5	0.9	1.9	3.9	3.6	0.6	2.0	2.8	1.8	6.7	1.2	0.9

Tidal currents for M_2 and S_2 constituents are clearly identifiable in the power spectra of depth-average velocity (Fig. 9). Results suggest that major semi-axis length at 20 m is about 11–12 cm/s, and reduces to 3.9–6.7 cm/s at 100 m (Figs. 10a and 11a, and Table 2). They are rotated from northeast-southwest direction at 20 m to north-south direction at 100 m (Figs. 10a and 11a). Rotary coefficient indicates that both M_2 and S_2 tidal currents exhibit clockwise rotation throughout the water column (Figs. 10b and 11b). It is exceptional for N_2 and K_1 tidal currents that have counter-clockwise rotation below 40 m during NEM season (Figs. 10b and 11b). Compared between seasons, the current is slightly stronger during SWM season than during NEM season.
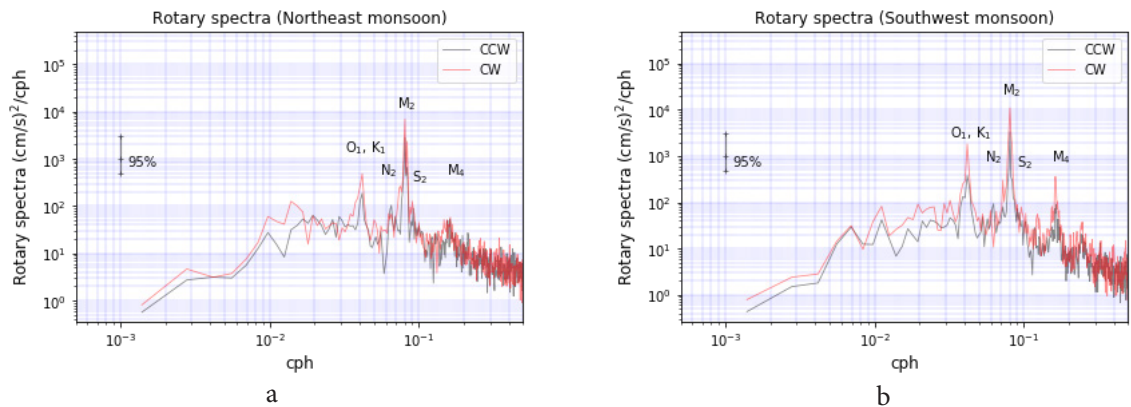

Figure 9. (a) Rotary spectra of high-pass filtered velocity during Northeast monsoon season and (b) Southwest monsoon seasons with respect to frequencies in cycle per hour (cph). CCW denotes counterclockwise rotation (blue) and CW is clockwise rotation (red).
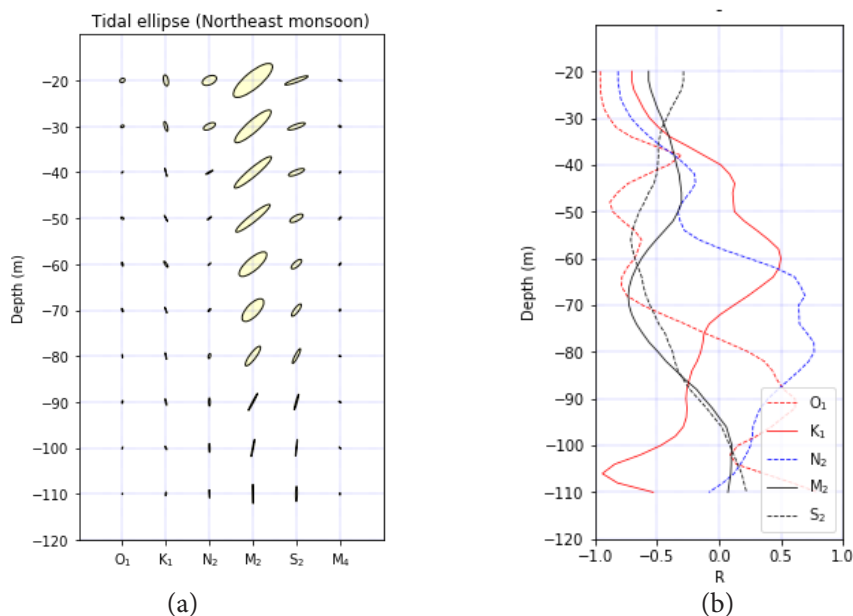

Figure 10. (a) Tidal ellipses for O_1, K_1, M_2, S_2, and M_4 tidal constituents derived by applying rotary spectral method to high-pass filtered velocity and (b) associated rotational coefficient for each dominant tidal constituents during Northeast monsoon season.
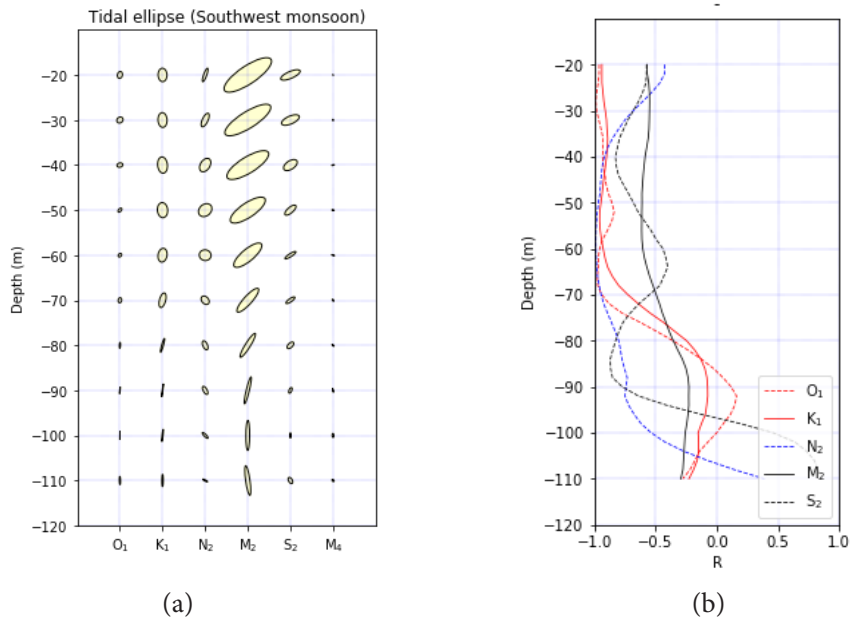
(a)　　　　　　　　　　(b)

Figure 11. (a) Tidal ellipses for O_1, K_1, M_2, S_2, and M_4 tidal constituents derived by applying rotary spectral method to high-pass filtered velocity and (b) associated rotational coefficient for each dominant tidal constituents during Southwest monsoon season.

CONCLUSION

The Asian monsoon prevailing over the AS causes seasonal variation in coastal sea level as evidenced in the observations both at the ADCP-mooring station and the tide-gauge station at Taphao Noi Island. The sea level was low during NEM season associated with northerly wind, and high during SWM season associated with southerly wind. In addition to monsoon, coastal sea level in the AS is also influenced by remote factors from the EEIO as shown in the observation made in December.

Low-frequency current is primarily in north-south orientation. It has a baroclinic-like structure with prominent meridional velocity shear around 50 m. Depth-averaged velocity in the upper layer shows weak seasonality with intermittent reversal. Without remote interference, southward current is typical during NEM season with strongest current in January. Northward flow, on the other hand, is observed in June and July during SWM season. Northward flow associated with elevating coastal sea level observed in December could be induced by westerly equatorial zonal wind stress over

EEIO. This underlines connection between these two regions. Nevertheless, this distinct northward flow still needs verifying with theory and numerical model.

CTD was casted in November 2018 before the ADCP deployment and in April 2019 during the observation period. Based on T-S diagram, the Andaman shelf experiences two water masses seasonally. Precipitation is high along southwestern Malaysian Peninsula especially during the last quarter of a year, and the largest river input from the north (*e.g.*, Irrawaddy River) supplies tremendous amount of fresh water that accumulates in the interior, thus we attribute low-salinity water in November both freshwater sources. In April, the shelf is influenced by off-shelf water which increases surface salinity. Stratification is prominent at 50 m in both months but stronger in April. It is worth noting that water mass with density exceeding 1022.5 kg/m3 was observed only in April, and is likely sustained by a shallower isothermal layer.

Tide is an important oceanographic process at play on the Andaman shelf. Analysis of sea level and tidal current suggests that semi-diurnal M_2 tide is the most predominant tidal constituent, followed

by S_2 tide. N_2 and K_1 tides contribute equally to sea level variation. However, weak shallow water constituent, M_4, is negligible on the shelf. Applying rotary spectral estimation, clockwise-rotating tidal current is indicated for most of tidal constituents. Major semi-axis angles of M_2 and S_2 tides rotate from northeast direction at 20 m to the north near the bottom. The current is slightly stronger in SWM season than in NEM season.

REFERENCES

Andersen, O.B. 1999. Shallow water tidal determination from altimetry - the M_4 constituent. Boll. Geof. Teor. Appl. **40:** 427–437.

Angsakul, K., M. Jaroensutasinee and K. Jaroensutasinee. 2007. Numerical Study of Principal Tidal Constituents in the Gulf of Thailand and the Andaman Sea. Walailak J. Sci. & Tech. **4(1):** 95–109.

Bonjean, F., and G.S.E. Lagerloef. 2002. Diagnostic model and analysis of the surface currents in the tropical Pacific Ocean. J. Phys. Oceanogr. **32:** 2938–2954.

Caldwell, P. C., M. A. Merrifield, P. R. Thompson. 2015. Sea level measured by tide gauges from global oceans - the Joint Archive for Sea Level holdings (NCEI Accession 0019568), Version 5.5, NOAA National Centers for Environmental Information, Dataset, [DOI:10.7289/V5V40S7W]

Carlson, D.F., and A.J. Clarke. 2009. Seasonal along-isobath geostrophic flows on the west Florida shelf with application to *Karenia brevis* red tide blooms in Florida's Big Bend. Cont. Shelf Res. **29:** 445–455.

Chatterjee A, D. Shankar, J.P. McCreary, P.N. Vinayachandran and A. Mukherjee. 2017. Dynamics of Andaman Sea circulation and its role in connecting the equatorial Indian Ocean to the Bay of Bengal. J. Geophys. Res. **122(4):** 3200–3218.

Chelton D.B., R.A. Deszoeke and M.G. Schlax. 1999. Geographical variability of the first baroclinic Rossby radius of deformation. J. Phys. Oceanogr. **28:** 433–459.

Clarke, A.J. 1983. The reflection of equatorial waves from oceanic boundaries. J. Phys. Oceanogr. **13(7):** 1193–1207.

Clarke, A.J. and X. Liu. 1993. Observations and dynamics of semiannual and annual sea levels near the eastern equatorial Indian Ocean boundary. J. Phys. Oceanogr. **23:** 386–399.

Delcroix, T., G. Eldin, M. McPhaden, and A. Morlière. 1993. Effects of westerly wind bursts upon the western equatorial Pacific Ocean, February–April 1991. J. Geophys. Res. **98:** 16379–16385.

Elipot, S. and R. Lumpkin. 2008. Spectral description of oceanic near-surface variability. Geophys. Res. Lett. **35(5):** https://doi.org/10.1029/2007GL032874.

Emery, W.J. and R.E. Thomson. 2001. Data Analysis Methods in Physical Oceanography. 2nd Edition. Elsevier Science. 654 pp.

Gille, S.T., and C.W. Hughes. 2001. Aliasing of high-frequency variability by altimetry: Evaluation from bottom pressure recorders. Geophys. Res. Lett. **28(9):** 1755–1758.

Gilmour, A.E. 1987. A preliminary rotary spectral analysis of inertial currents off the west coast of New Zealand (Note). New Zealand Journal of Marine and Freshwater Research **21:** 353–357.

Ghaffari, P. and V. Chegini. 2010. Acoustic Doppler Current Profiler observations in the southern Caspian Sea: shelf currents and flow field off Feridoonkenar Bay, Iran. Ocean Sci. **6:** 737–748.

Godin, G. 1972. The Analysis of Tides. University of Toronto Press, Toronto. 264 pp.

Gonella, J. 1972. A rotary-component method for analysing meteorological and oceanographic vector time series. Deep-Sea Res. Oceanogr. Abstr. **19(12):** 833–846.

Kalnay, E., M. Kanamitsu, R. Kistler, W. Collins, D. Deaven, L. Gandin, M. Iredell, S. Saha, G. White, J. Woollen, Y. Zhu, M. Chelliah, W. Ebisuzaki, W. Higgins, J. Janowiak, K.C. Mo, C. Ropelewski, J. Wang, A. Leetmaa, R. Reynolds, R. Jenne, and D. Joseph. 1996. The NCEP/NCAR 40-year reanalysis project. BAMS. **77(3):** 437–470.

Le Provost, C. 1991. Generation of overtides and compound tides. **In:** B. B. Parker (ed). Tidal Hydrodynamics. John Wiley, New York. pp. 269–295

Levitus, S. 1982. Climatological atlas of the world ocean, U.S. Government Printing Office 13, NOAA, Washington, D.C., 163 pp.

Liu, Y., J. Guo, H. Wang, Y. Xue, S. Khokiattiwong and W. Yu. 2018a. The observed tidal and residual currents in the Andaman Sea during the second half of 2016. Acta Oceanol. Sin. **37(9):** 13–21.

Liu, Y., K. Li, C. Ning, Y. Yang, H. Wang, J. Liu, S. Khokiattiwong and W. Yu. 2018b. Observed Seasonal Variations of the Upper Ocean Structure and Air-Sea Interactions in the Andaman Sea. J. Geophys. Res. **123:** 922–938.

Liu, Y., and R.H. Weisberg. 2005. Momentum balance diagnoses for the West Florida Shelf. Cont. Shelf Res. **25:** 2054–2074.

Mahadevan, A., G. Spiro Jaeger, M. Freilich, M. Omand, E.L. Shroyer and D. Sengupta. 2016. Freshwater in the Bay of Bengal: Its fate and role in air-sea heat exchange. Oceanography **29(2):** 72–81. [http://dx.doi.org/10.5670/oceanog.2016.40.]

McCreary, J. 1976. Eastern Tropical Ocean Response to Changing Wind Systems: with Application to El Niño. J. Phys. Oceanogr. **6(5):** 632–645.

McDougall, T.J. and P.M. Barker 2011. Getting started with TEOS-10 and the Gibbs Seawater (GSW) Oceanographic Toolbox. SCOR/IAPSO WG127. 28 pp.

Mohanty, S., A.D. Rao and G. Latha. 2018. Energetics of Semidiurnal Internal Tides in the Andaman Sea. J. Geophys. Res: Oceans **123:** 6224–6240.

Peng, S., J. Liao, X. Wang, Z. Liu, Y. Liu, Y. Zhu, B. Li, S. Khokiattiwong, W. Yu. 2021 Energetics-Based Estimation of the Diapycnal Mixing Induced by Internal Tides in the Andaman Sea. J. Geophys. Res: Oceans **126(4):** 1–17. [https://doi.org/10.1029/2020JC016521]

O'Brien, J.J. and R.D. Pillsbury. 1974. Note and correspondence: Rotary wind spectra in a sea breeze regime. J. Appl. Meteorol. **13:** 820–825.

Sangmanee C., V. Vasinamekhin, and S. Khokiattiwong. 2020. Water characteristic in the south Andaman shelf sea from observations during 2014–2019. Phuket mar. biol. Cent. Res. Bull. **77:** 75–85.

Ray, R.D. 2007. Propagation of the overtide M4 through the deep Atlantic Ocean. Geophys. Res. Lett. **34(21):** L21602.

Volkov, D.L., G. Larnicol, and J. Dorandeu. 2007. Improving the quality of satellite altimetry data over continental shelves. J. Geophys. Res: Oceans **112.** [https://doi.org/10.1029/2006JC003765.]

Wall, M, G.M. Schmidt, P. Janjang, S. Khokiattiwong and C. Richter. 2012. Differential impact of monsoon and large amplitude internal waves on coral reef development in the Andaman Sea. PLoS One, **7(11)**.

Wall, M., L. Putchim, G. M. Schmidt, C. Jantzen, S. Khokiattiwong and C. Richter Walls. 2015. Large-amplitude internal waves benefit corals during thermal stress. Proc. R. Soc. B. **282(1799):** 20140650.

Walters, R.A., and F.E. Werner (1991), Nonlinear generation of overtides, compound tides, and residuals, **In:** B. B. Parker (ed.) Tidal Hydrodynamics. John Wiley, New York. pp. 297–320

Welch, P. 1967. The use of fast Fourier transform for the estimation of power spectra: A method based on time averaging over short, modified periodograms. IEEE Transactions on Audio and Electroacoustics **15(2):** 70–73.

Yang, H., and R.H. Weisberg. 1999. Response of the West Florida Shelf circulation to climatological wind

stress forcing. J. Geophys. Res. **104:** 5301–5320.

Yi-Neng, L., S.-Q. Peng and X.-Z. Zeng. 2012. Observations and Simulations of the Circulation and Mixing around the Andaman-Nicobar Submarine Ridge. Atmospheric and Oceanic Science Letters **5(4):**